5

Chapter

System verification and validation

The chapter starts off with the definition of verification and validation as it is interpreted in the context of this project. The focus is shifted to system verification and validation, which include nondestructive inspections. Findings from the inspections are interpreted and a finite element (FE) model is implemented to investigate the stress implications. The chapter is concluded with the interpretation of the results and recommendations.

5.1 Context

Verification and validation is defined in [52] as:

"...verification is to ensure that selected work, products meet their specified requirements."

"...validation is to demonstrate that a product or product component fulfils its intended use when placed in its intended environment."

One form of system verification would be to measure the dynamic stress in the IM rotor section at maximum operating conditions and comparing the results to the maximum stress specified in the design specifications. However, due to the nature of the system, it is very difficult, if at all possible, to measure the dynamic stress in the rotor. From this point of view a system was put in place in chapter 3, where the design tool used to calculate the dynamic stress is systematically verified and validated. Verification of the tool is done by comparing the analytically calculated stress to the stress calculated using a finite element analysis (FEA). Practical strain gage measurements were in turn used to validate the FEA design tool.

Another form of validation on a sub-system level documented in chapter 3, was measuring the diameter growth at the bar outer diameter (OD) due to the dowel pin insert and comparing the results to the nonlinear FEA. The electrical contact resistance at the end ring/bar interface was also measured to validate the decision to use this type of connection.

The purpose of this chapter is to conclude the verification and validation on a system level. In this chapter nondestructive inspection methods are investigated, which can be implemented to inspect the rotor before and after operation. This will validate that the rotor can successfully be operated at its

designed conditions. The nondestructive inspections methods investigated includes, liquid penetration, magnetic-particle, ultrasonic, acoustic, radiology, eddy-current, dimensional and visual inspection.

The results from the nondestructive inspections are described and any discrepancies are evaluated and interpreted using both analytical calculations and FEA. The chapter ends with a conclusion that summarises the effect of any discrepancies

5.2 Nondestructive inspection methods

Before the assembly of the rotor into the stator could commence the induction machine (IM) rotor section should be inspected. This section describes some of the nondestructive inspection processes available and the suitability of these inspections on the IM rotor section.

5.2.1 Liquid penetration inspection

In liquid penetration inspection, the component is cleaned and dried after which a liquid penetrant is applied to the surface of the component. The component's surface is water-washed to remove the excess liquid penetrant, after which a developing agent is applied. The defect/crack is then revealed. This type of inspection can reveal discontinuities as small as 0.1 µm. This technique is however limited to detecting surface defects only [13].

5.2.2 Magnetic-particle inspection

Magnetic particle inspection is limited to ferromagnetic materials. The component is covered in fine ferromagnetic particles and a current is applied to the component. The current causes a magnetic field and a defect causes the particles to bundle around the discontinuity. The technique reveals surface as well as subsurface defects [13].

5.2.3 Ultrasonic inspection

Ultrasonic inspection involves transducers creating an ultrasonic beam that travels through the component. When the beam encounters a defect, a fragment of the ultrasonic energy is reflected and the position and size of the defect is determined by the time delay and amplitude of the reflected energy. This technique can be applied to relatively large components and the same component can be inspected from different positions to determine the positions of internal defects [13].

5.2.4 Acoustic inspection methods

Acoustic-emission is the monitoring of signals produced by the component itself. The signal is produced due to plastic deformation, crack initiation or phase transformation to name but a few. Usually the component inspected is subjected to elastic deformation, for instance; bending a beam or applying a torque to a shaft. The acoustic-emissions are detected by sensors, constituting piezoelectric ceramic elements. This technique is typically used for continuous monitoring of critical components [13].

5.2.5 Radiography

Radiography uses x-rays to detect defects. The technique is based on detecting a change in density. Furthermore, defects and its immediate surrounding material are normally denser than the rest of the component's material. The defect is therefore visible on the x-ray film in the form of a lighter shade compared to the rest of the component's material. The most recent computed tomography, replaces film with a linear array of detectors. As the component is rotated and moved vertically the detectors sample radiation and thin cross sections of the component are shown as x-ray images. These images are used to inspect the component. However, this technique requires expensive equipment and skilled technicians to interpret the results [13].

5.2.6 Eddy-current inspection

Eddy-current inspection involves using an electric coil connected to alternating current. The component is placed in or near the coil and eddy currents are generated in the component. Any defect causes a change in the eddy current direction and excites the inspection coil. A defect is detected by a change in the measured inspection coil's voltage. The inspection coil can be altered to accommodate any required shape and a change in voltage indicates a defect. However, the component is required to be electrically conductive and the defects detected can be up to 13 mm deep [13].

In summary, all of the inspection methods discussed above is only applicable to individual components. The fact that the IM rotor section comprises different materials with varying densities eliminates the use of all of the inspection methods discussed above. From this point of view dimensional measurement and visual inspection is the only viable nondestructive inspection methods. Furthermore, the materials used are procured with material certificates.

In the next section the final dimensions of each component is documented and used in to calculate the expected stresses in the final product. The FEM calculated stress will verify that the rotor fulfils the design specifications.

5.3 Stress analysis of IM rotor section with final measured dimensions

After final machining each component is inspected and measured using a high precision measuring equipment in a temperature controlled room at Denel Dynamics Pty Ltd. The measured dimensions are displayed in Table 5-1. With the actual dimensions of each of the components know, the expected stresses in the built IM rotor section can be calculated, using the systematically verified and validated FE model. The calculated stress is however, for the ideal case, where the assembly procedure does not influence the stresses in the rotor. It is also recognised that, although extensive effort was put in to ensure accurate measurements, all measurement will have a tolerance.

Table 5-1 shows both the measured and theoretically calculated interference at each interface. All the measured interferences are within the allowable dimensional tolerance except for the "spacer remade" as discussed in chapter 4. The variance in dimension is due to the capabilities of the manufacturing shop used for the manufacturing of the new spacer. However, the increase in interference does not have an effect on the minimum FOS due to the high yield strength of the spacer material.

Table 5-1: Tabulated final measured dimensions

Component	Measured values			Theoretical values	
	ID (mm)	OD (mm)	Interference (µm)	Min Interference (µm)	Max Interference (µm)
Shaft	0	80.060	N/A	N/A	N/A
Lamination	79.988	123.0	72	70	76
Spacer	79.988	123.0	72	70	76
Spacer remade	79.976	123.0	84	70	76
End rings	79.905	123.0	155	150	156
Conductive bar slots	N/A	10.006	N/A	N/A	N/A
Conductive bar dowel end	0	10.030[13]	24	10	30
Conductive bar parallel fit end	0	10.020	14	10	30

With the actual dimensions known, each component is modelled according to these dimensions and the complete IM rotor section FEA is run. Figure 5-1 illustrates a FOS fringe plot of the complete assembly under the worst loading condition. The results indicate a minimum FOS of 2.06 which is more than the minimum FOS of 2.

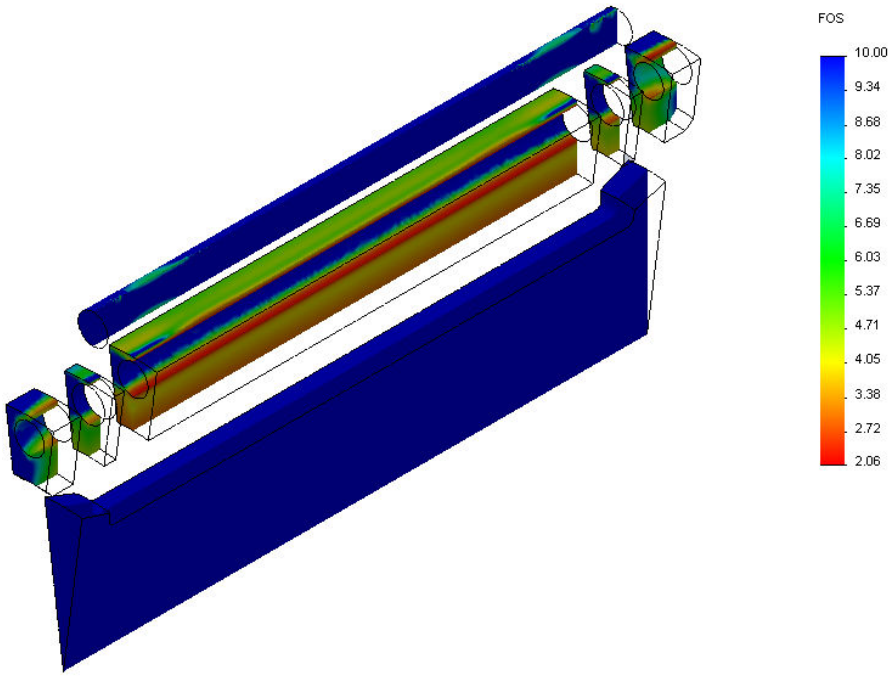

Figure 5-1: FOS plot of the IM rotor section with actual interferences at maximum operating conditions

[13] Initial OD of the bar is 9.995 mm. After the insertion of the dowel the OD increased by a maximum of 35 µm.

Using the same FE model the contact pressure (CP) at the interfaces is calculated as illustrated in Figure 5-2. The results show the contact pressure at each component, which indicates no loss in contact at any of the interfaces.

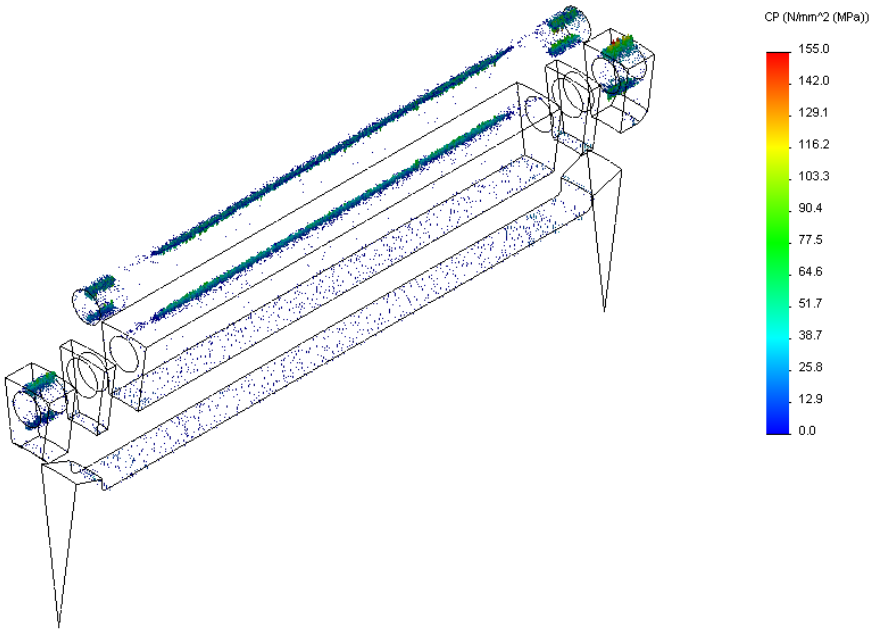

Figure 5-2: IM rotor section's CP at maximum operating conditions with actual measured interference

Table 5-2 summarises the CP at the interfaces of each component. The results indicate the minimum, maximum and average CP at each interface of the actual measured interference. The large variation between the minimum and maximum CP is due to stress concentrations at the edges of the components resulting in a high CP at these locations.

Table 5-2: Summary of CP at the individual component interfaces

Component	Actual interference, CP (MPa)			Theoretically minimum interference, CP (MPa)
	Min	Max	Average	Average
End ring L	0	15.737	4.138	5.03
Spacer L	2.031	24.529	10.232	12.64
Laminations	1.306	23.703	6.838	6.16
Spacer R	3.343	43.837	18.469	12.64
End ring R	0	36.416	4.958	5.03

The average CP of the theoretical minimum interference is also included. In theory the average CP of the measured interference should be higher, but not by much due to the small difference in interference, than the average CP of the minimum interference. This is illustrated by the lamination's average CP, where the average CP of the actual interference is 10 % higher compared to the average CP of the theoretical minimum interference. However, this is not the case in the average CP of the laminations

and spacer L. In these cases the average CP of the actual interference is less compared to the average CP of the theoretical minimum interference.

This can be attributed to the difference in number of mesh elements on the surface area of the interfaces. Due to the relatively large lamination surface, the average CP will be a better representation of the actual CP at the interface because a few stress concentrations at the edges will be nullified. However, with the end rings and spacers having much smaller contact areas the stress concentrations could influence the average significantly. For this reason a trim mean value of the CP would be a more accurate comparison. The fact that the interference of the components in the two FE models has a small difference (2 – 4 μ), reinforces the fact that any difference in mesh, causing some stress concentrations at the edges of the components, will affect the calculate average CP. Especially the component's with a small interface area.

Notice, however, that the average of each component is more than zero, indicating no loss in contact at the interfaces. The difference in CP of the two spacers is due the assembly problem as discussed in detail in Chapter 4.

The FEM results verify that the actual IM rotor section will have a FOS of more than 2 at the maximum operating conditions while maintaining an average CP above zero. However, these results are for the ideal assembly conditions, which was not the case. The following section describes the final inspection before the IM is assembled.

5.4 Visual inspection findings

After final machining and balancing a visual inspection of the IM rotor revealed that the end ring was displaced axially, with the maximum displacement at the OD of about 0.5 mm as indicated in Figure 5-3. The displacement is only noticeable at the bar/end ring interfaces, where it can be seen that the face of the end ring and conductive bar is no longer parallel. On the other hand Figure 5-4 illustrates that there is no visible gap on the outer surface of the rotor between the individual components.

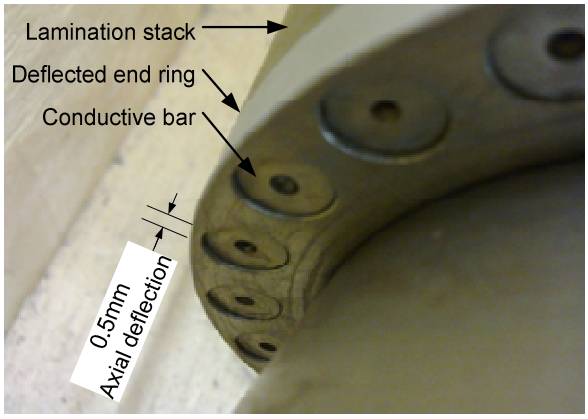

Figure 5-3: Illustration of the axial displacement of the end ring

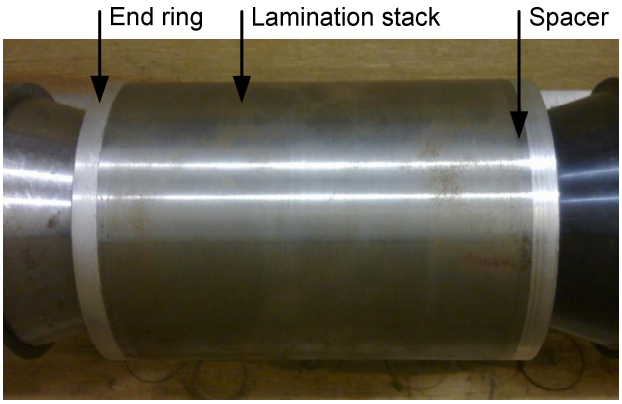

Figure 5-4: IM rotor section after final machining

Possible causes of the axial displacement include: buckling due to the relatively large interference fit or the axial cutting force produced by the final machining. These issues are investigated in the following sections.

5.4.1 Buckling of a shrink fitted lamination disc

J.D. Herbst et al. [9] describes that buckling of the shrink fitted components have to be considered in the design. This is especially important in high speed applications where large interference is required. The OD to ID ratio of the lamination disc is the main consideration in conical buckling and with an OD/ID ratio of about 4.5 for the J.D. Herbst et al. rotor, conical buckling is considered. The rotor described in this dissertation has however, an OD/ID ratio of 2.18, before final OD machining and indicates a very small chance of conical buckling. None the less, due to the axial displacement of the end ring, conical buckling has to be considered.

Using a FE model of a single lamination disc, as shrink fitted onto a shaft, the critical CP required for the disc to buckle is calculated. Figure 5-5 illustrates the first (a) and second (b) conical buckling modes, which will only occur at a CP of 1650 and 3855 MPa respectively. The CP can be translated to a critical interference δ_d of 2.18 mm for the first mode, which is enormous. When combining the CP and tangential stress, the Von Mises stress at the shaft/lamination interface is calculated to be in excess of 3300 MPa. This is more than seven times higher than the laminations' yield strength of 450 MPa. The results indicate that the critical failure mode is not buckling and that the lamination material will yield long before buckling occurs. Considering a single lamination is also conservative because a clamping jig was used to clamp the IM rotor section during the shrink fit process.

However, the critical buckling load described above only incorporates the radial load due to the interference fit. Another consideration should be, the axial force applied by the final machining process of the rotor OD.

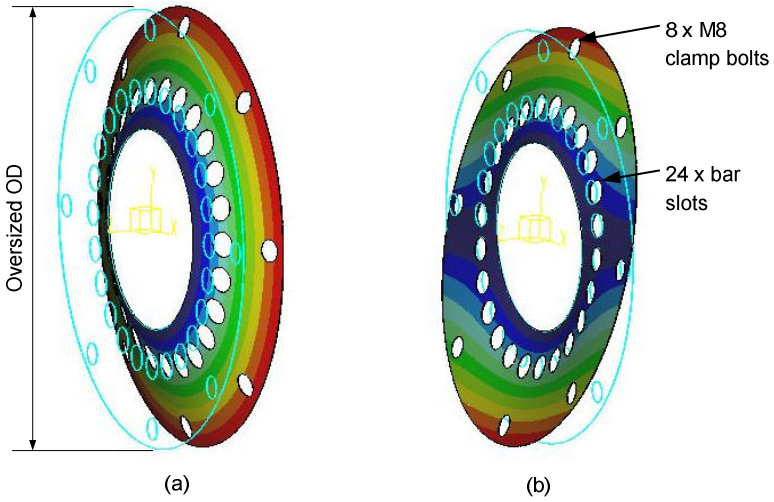

Figure 5-5: Illustration of a single lamination disc's first and second conical buckling modes: (a) isometric view of first model (*CP* =1650 MPa), (b) isometric view of second model (*CP* =3855 MPa).

5.4.2 Cutting forces

In order to investigate the effect of the axial force due to the final machining of the OD, the cutting forces due to the machining process are calculated. Some of the variables and equations required to calculate the forces are illustrated in Figure 5-6. The variables of interest, when calculating cutting forces are: depth of cut *a* (mm), equivalent chip thickness *ECT* (mm), chip follow angle *CFA* (°), chip edge length CEL (mm), feed rate *f* (mm/rev) and cutting speed *V* (m/min) [53]. However, none of these variables were measured or documented during the machining process.

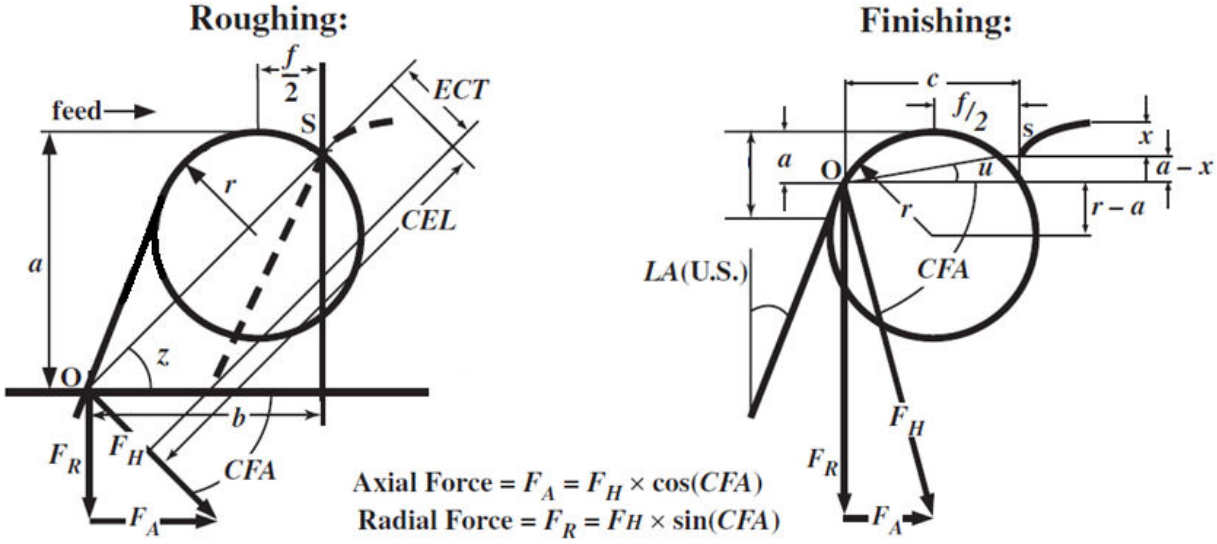

Figure 5-6: Illustration of parameters and equations for calculating cutting forces [53]

If the power P_m (kW) of the lathe is known and recommended feeds and speeds are used the expected cutting forces can be calculated. The suggested cutting speed and feed for alloy steel with a Brinell Hardness of between 125 – 175 is given as $f \approx 0.4318$ mm/rev and $V \approx 160$ m/min. From these variables the metal removal rate Q (cm^3/s) can be calculated with (5.1), for a variety of cut depths. From [53] the power constant K_p is given as 1.72 with a feed factor C of 0.84, W tool wear constant of 0.84 and machine tool efficiency e of 80 %. Substituting (5.1) into (5.2) the required powers for the variety of cut depths are calculated as illustrated in Figure 5-7.

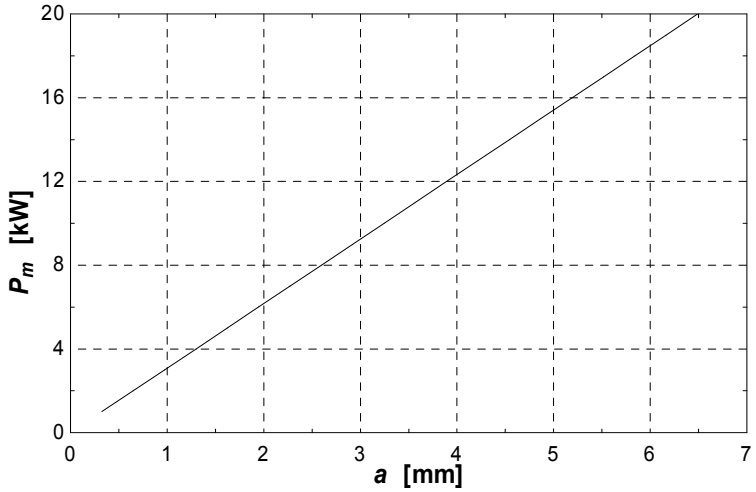

Figure 5-7: Calculated required power for a depth of cut

$$Q = \frac{V}{60} f \times a \tag{5.1}$$

$$P_m = \frac{K_p CQW}{e} \tag{5.2}$$

With the feed rate known, the chip cross sectional areas A is calculated from (5.3), for the range of cut depths. Selecting a *CEL* of 1.2 times the depth of cut, the *ECT* is calculated using (5.4) [53]. Due to the ratio of *CEL/a* being constant, *ECT* is a constant value of 0.333 mm. From the calculated *ECT,* the specific cutting Force K_c is found in Figure 5-8 and for *ECT* of 0.333 mm and V of 160 m/min K_c is selected as 1900 Mpa.

$$A = f \times a \tag{5.3}$$

$$ECT = \frac{A}{CEL} \tag{5.4}$$

With both the specific cutting force and chip cross sectional area known, the tangential cutting force F_c is calculated using (5.5). In order to calculate the axial cutting force F_A and radial cutting force F_R, the resultant force F_H is required. F_H is calculated in (5.6), where a force ratio (*FH/FC*) found from Figure 5-9 is multiplied with the calculated tangential force [53].

$$F_c = A \times K_c \tag{5.5}$$

$$F_H = \frac{FH}{FC} \times F_c \tag{5.6}$$

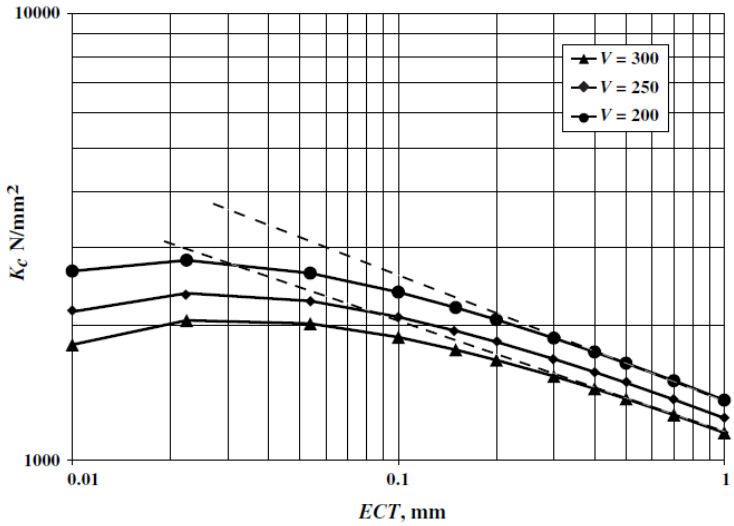

Figure 5-8: Calculated ratio between *ECT* and K_c for different cutting speeds [53]

After calculating F_H and with a chip flow angle of 30°[14], the axial force is calculated in (5.7) [53]. The calculated axial force is dependent on the depth of cut and increases as *a* is increased, as illustrated in Figure 5-10. From Figure 5-7 it is apparent that for a depth of cut of 6,5 mm the power required is 20 kW. From that the axial force is calculated to be 1550 N as shown in Figure 5-10. The lathe used during final machining was about 12 kW, resulting in a maximum axial force of 920 N, at the current cutting parameters. However, the forces are dependent on assumptions and could be more than the 920 N. Therefore, the maximum force used is assumed to be 1550 N and is a conservative estimation.

$$F_A = F_H \times \cos(CFA) \tag{5.7}$$

[14] Prescribed chip flow angle for roughing [**53**]

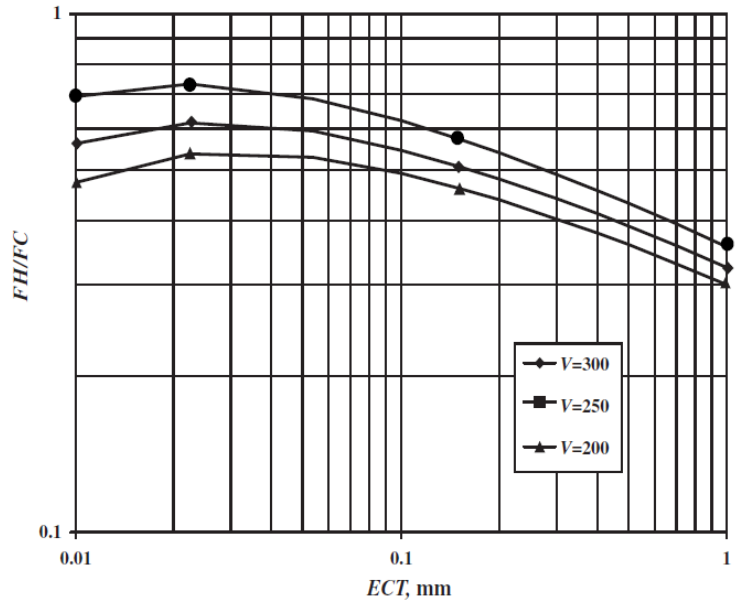

Figure 5-9: Illustration of ratio between cutting forces at different cutting speeds [53]

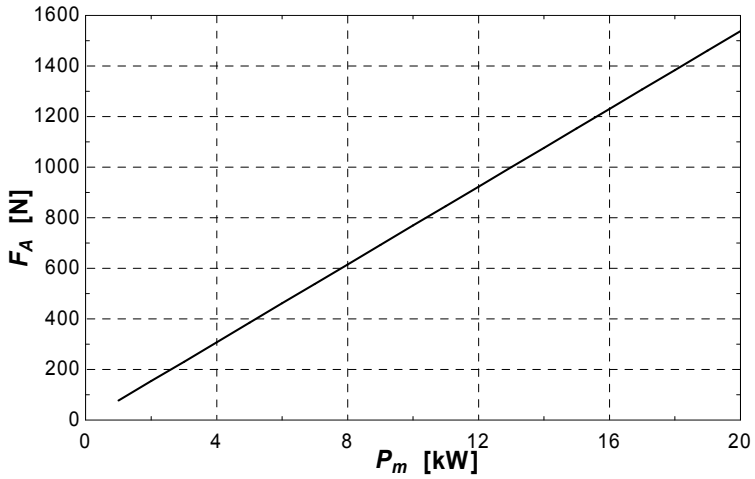

Figure 5-10: Calculated required power for a specific axial force

The largest possible axial force as calculated in this section is relatively small compared to the force required to deflect the IM rotor section. A simplified FE model shows that a axial force of 5400 N is required to deflect the end ring 0.5 mm alone, this is without the additional stiffness added by the lamination stack. From these results the axial cutting force is shown to be small compared to the force required to deflect the IM rotor section.

The results indicate that the end ring's axial deflection cannot be due to conical buckling or the axial force applied by the final machining operation. However, the question remains, why the end ring is deflected if the calculations clearly show that the IM rotor section will not buckle or deflect under these conditions. The fact that the end ring is permanently displaced supports the investigation of permanent

deformation. A detail stress analysis is conducted using a revised FE model as described in the following section.

5.5 Stress due to IM rotor section axial deflection

Investigating the effect of the end ring deflection, on the maximum stress in the assembly, requires a new FE model. Looking at Figure 5-4, it is clear that there are no gaps visible on the outer surface of the rotor section and that the lamination stack, spacers and end rings are continuous. This presents the question of, what is causing the end ring to deflect and not return to its initial position and why is there no gap visible even though the two end rings are displaced in opposite directions.

After enquiring with the manufacturer it was found that the lamination material did not machine easily. In fact the machinability was poor and the material tended to smear. This possibly, resulted in the lamination discs to form burrs and material is forced between the lamination discs. This will explain why, even though the end rings are deflected in opposite directions[15], the outer surface seems continuous.

With this in mind the axial deflection was simulated by modelling the lamination stack with the axial deflection at the ends as illustrated in Figure 5-11. The results shown in Figure 5-12 illustrate a minimum FOS of 0.6 on small sections of the end rings. The FOS of less than 1 implies that the material is stressed over its yield strength. However, the maximum stress is concentrated on a very small area as illustrated in Figure 5-13 and should be investigated further before any conclusions can be drawn. Furthermore, apart from the relatively small sections with the 0.6 FOS and an area where the FOS is between 1 and 1.15, most of the components have a FOS of more than 2. For this reason permanent deformation of the end rings are ruled out.

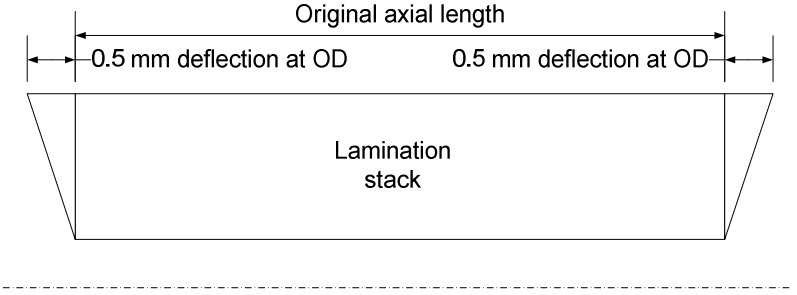

Figure 5-11: A side view of an exaggerated illustration of the axial deflection of the lamination stack

Upon investigating the influence of changing the mesh element size, it was found that the stress at these small areas does not converge. Indicating that the node points of the two surfaces at the contact area does not match. The fact that the maximum stress increases, while the visible stress concentration area decreases, as the mesh size is decreased, also indicate that the maximum stress is due to a mesh problem and should be verified.

[15] Material is removed in both axial directions during the turning process

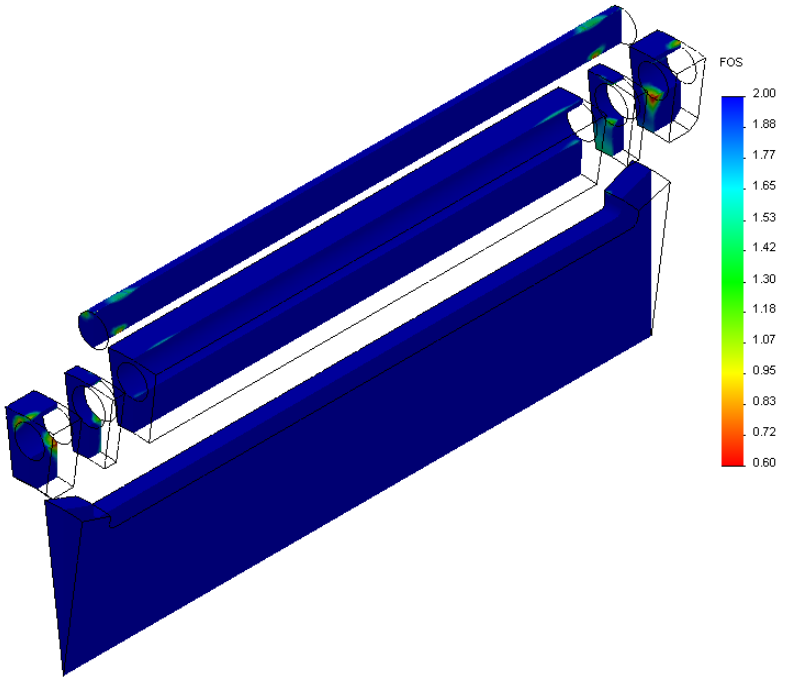

Figure 5-12: FOS fringe plot of the axially deflected lamination stack assembly

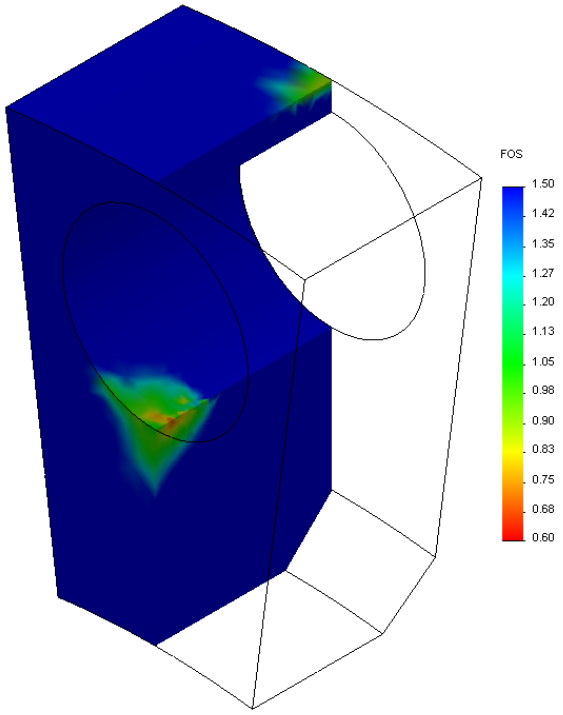

Figure 5-13: Detailed view on the FOS plot of the end ring

In order to verify the maximum stress found from the FEM results shown in Figure 5-12 and Figure 5-13, the maximum stress is calculated analytically. Figure 5-14 illustrates a side view of a section of the IM

rotor. The result shows the CP distribution at the stress concentration area found at the bottom of the end ring/bar interface. The reaction force F_R, due to the axial deflection of the end ring, is measured in the simulation and is used to analytically calculate the stress at the end ring/bar interface.

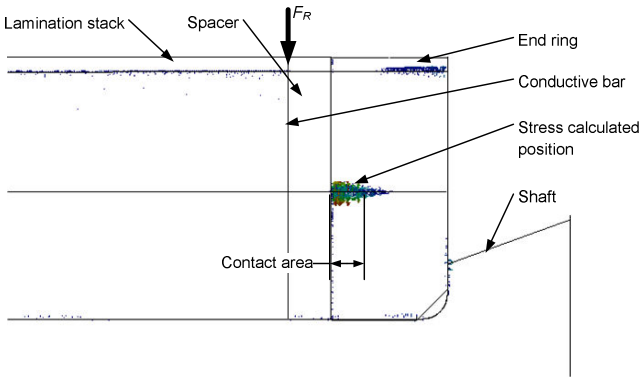

Figure 5-14: Side view of CP distribution

Three stress components are contributing to the stress at the contact area as illustrated in Figure 5-14. The first stress component is the tangential stress due to the shaft/end ring and the end ring/conductive bar shrink fits. The second stress component is the radial stress due to the same shrink fits. These stresses are measured in the FEM simulation of the actual measured dimensions with no axial deflection.

The third component contributing to the stress is the bearing stress due to the reaction force on the conductive bar, as the end ring is axially deflected (bended). Although the force distribution at the interface due to the reaction force F_R is rather complex, it can be represented by the distribution as illustrated in Figure 5-15 (a). In order to translate the force into a stress, the area is required where the force is applied. The non-uniform force distribution as illustrated in Figure 5-15 (a), makes it difficult, however, the force distribution is assumed to be distributed as illustrated in Figure 5-15 (b). Assuming the force distribution, due to the moment, is uniform on only a quarter of the axial length.

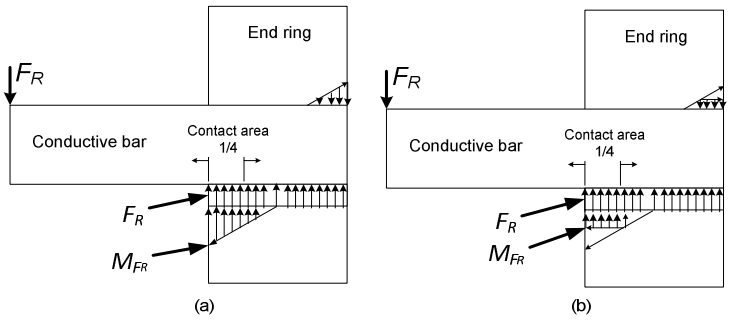

Figure 5-15: Illustration of (a) actual distribution, (b) assumed distribution of force due to reaction force F_R

Furthermore, the bearing stress distribution due to the reaction force is investigated as illustrated in Figure 5-16. Normally the force is applied to the projected area of the round to calculate the average

stress over the area and is represented by the “Average stress” line in Figure 5-16. However, in reality the force distribution is in the form of the “Measured stress distribution” line shown in Figure 5-16. The measured stress distribution is found from a FE model where the bar and slot is both 10.0 mm in diameter and friction is ignored. From these results the maximum stress on the area is measured to be -35 MPa, which is 1.4 times more than the average. Using the 1.4 concentration factor K_B, the maximum stress at the root of the bar slot is analytically calculated in the remainder of the section.

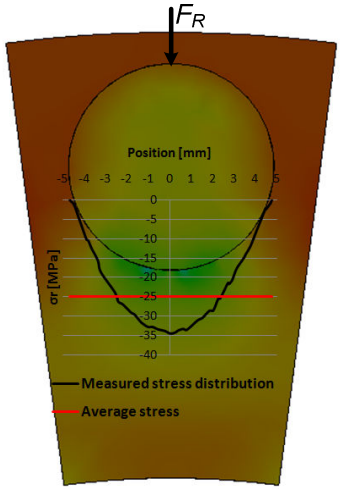

Figure 5-16: Bearing stress distribution

The forces produced by the deflection of the end ring are illustrated in Figure 5-17, the contact areas, ¼ of the total end ring axial length, are represented by the blocks numbered 1 and 2. Assuming the reaction force F_R is evenly distributed over the length of the end ring (9.5 mm) and the reaction forces due to the moment M_{FR} is evenly divided between the two areas. From this it is apparent that area 1 will be subjected to a force of $F_R/4$ plus $M_{FR}/2$ as calculated in (5.8). The corresponding radial stress due to these forces is calculated in (5.9) while incorporating the bearing stress concentration factor K_B.

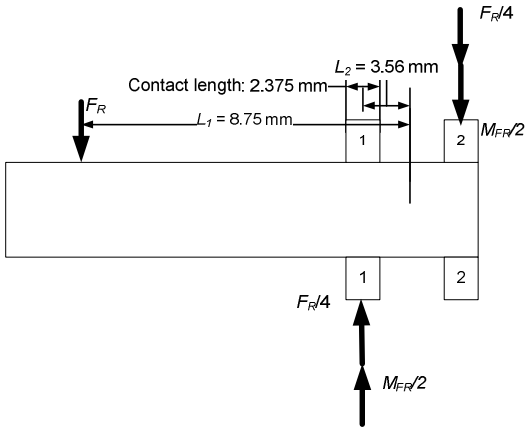

Figure 5-17: Illustration of reaction forces present due to the deflection

$$
\begin{aligned}
F_{R\_total} &= \frac{F_R}{4} + \frac{M_{FR}}{2} \\
&= \frac{F_R}{4} + \left[\frac{(F_R \times L_1)/(L_2)}{2} \right] \\
&= \frac{2447.66}{4} + \left[\frac{(2447.66 \times 0.00875)/(0.00356)}{2} \right] \\
&= \underline{3620 \ \text{N}}
\end{aligned}
\tag{5.8}
$$

$$
\begin{aligned}
\sigma_B &= K_B \frac{-F_{R\_total}}{A} \\
&= K_B \frac{-F_{R\_total}}{(2.375 \times 10)} \\
&= (1.4) \frac{-3620\text{N}}{(23.75\text{mm}^2)} \\
&= \underline{-213.4 \ \text{MPa}}
\end{aligned}
\tag{5.9}
$$

With all the individual stress components known, the total radial stress at contact area 1 is calculated in (5.10). The root of the bar slot will not be subjected to shear stress and therefore the maximum Von Mises stress can be calculated as shown in (5.11) followed by an analytically calculated factor of safety in (5.12). The analytic calculation indicates a higher FOS compared to the FEM results. The FEM maximum stress calculation is seen as conservative due to the relatively small area of the stress concentration.

$$
\begin{aligned}
\sigma_{R\_total} &= \sigma_B + \sigma_{R\_shrinkfit} \\
&= (-213.4) + (-50.81) \\
&= \underline{-264.2 \ \text{MPa}}
\end{aligned}
\tag{5.10}
$$

$$
\begin{aligned}
\sigma_{VM} &= \sqrt{{\sigma_{R\_total}}^2 - \sigma_{R\_total}\sigma_t + {\sigma_t}^2} \\
&= \sqrt{(-264.2)^2 - \left[(-264.2)(176.4)\right] + (176.4)^2} \\
&= \underline{384.04 \ \text{MPa}}
\end{aligned}
\tag{5.11}
$$

$$
\begin{aligned}
FOS &= \frac{\sigma_Y}{\sigma_{VM}} \\
&= \frac{516}{384.04} \\
&= \underline{1.344}
\end{aligned}
\tag{5.12}
$$

Since the maximum stress is below the materials yield strength, the contact pressure at the component's interfaces is investigated. Table 5-3 shows the results from the FEM analysis for the axial deflected end rings. The results indicate an increase in CP when compared to Table 5-2, however, this in reality does not seem possible. The increase can be attributed to stress concentrations at the edge of

the component, due to the bending. This is supported by the large increase in the maximum CP shown in the results.

Table 5-3: FEA calculated CP for axial deflected end ring simulation

Component	Contact pressure (MPa)		
	Min	Max	Average
End ring L	0	118.56	29.786
Spacer L	0	226.09	40.801
Laminations	0	80.341	2.347
Spacer R	0	266.91	45.748
End ring R	0	269.52	33.320

5.6 Assembly of induction machine

After establishing that the FEM calculated maximum stress for the axially deflected end ring model is incorrect, the decision was made to assemble the IM as shown in Figure 5-18 and continue with the test. The decision to go ahead with testing, even though the minimum FOS was below 2, was made from a project point of view. However, the testing is done in a safe and controlled environment. The tests facility is a steel reinforced concrete room and the IM is covered with 20 l water containers. The rotor was also spun up incrementally while monitoring multiple parameters, which would inform the operator of any irregularities. In this controlled environment the rotor was successfully spun up to the revised maximum design speed of 19,000 r/min.

Figure 5-18: Assembling the IM rotor into the stator

This was done a few times and the rotor was operated at the maximum speed for a relatively long time period. Although the motor was not tested under load, the extended test time period will enable the rotor to heat up to the design temperature. Under load the rotor will heat up to the design temperature in a shorter time period and be subjected to a 38 Nm torque. The additional torque is small and is not expected to influence the stress considerably. However, the motor should be tested under load and the rotor temperature should be monitored.

5.6.1 Disassemble and secondary inspection of rotor

After numerous tests including rotor delevitation tests[16] the rotor was removed from the stator and was visually inspected again. The inspection showed that nothing has changed and the deflection was exactly the same. The relative position of the conductive bars also did not change. The inspection results validate that the rotor can safely be operated at the design speed.

5.7 Conclusion

Verification and validation of the detail stress analysis of the IM rotor section is extremely difficult. Therefore, procedures are put in place to systematically verify and validate the "design tools" used in the detail design. From the detail design it is apparent that the dimensional tolerances of most of the components are critical. Effort was put in to manufacture each component to within the allowable tolerance.

After accurate measuring of the components, a finite element analysis is set up and used to verify that the IM rotor section fulfils the design requirements. However, with final inspection it is apparent that the end rings deflected axially after the final machining of the rotor's OD. Upon investigation of the results, it is proven that conical buckling is not the reason for the deflection. The axial force due to the machining of the OD is also investigated and shown to be small compared to the force required to deflect the end rings.

The conclusion is made that the machining process caused the lamination discs to form burrs and force material between the lamination discs, increasing the axial length of the stack at the OD. The deflection is incorporated in a new FE model and the results are interpreted. Initial FEM results present extremely high stress concentrations at the end ring/conductive bar interfaces. However, analytical calculations show that the IM rotor section has a minimum FOS of 1.34.

After evaluating the risk of a FOS below 2, the decision was made to incrementally spin the rotor while monitoring multiple parameters that could detect early signs of failure. The rotor was successfully spun to 19,000 r/min and multiple rotor delevitation tests were conducted at speeds of up to 10,000 r/min. After an adequate number of tests, the rotor was removed from the IM stator and re-inspected. During the inspection no irregularities were found and the IM was assembled and tested again.

[16] Also known as rotor drop tests. The tests and results are described in [**8**]